Vision, Modeling, and Visualization (2010), pp. 1–8

Convex Relaxation for Grain Segmentation at Atomic Scale

M. Boerdgen[1], B. Berkels[2], M. Rumpf[2] and D. Cremers[1]

[1]TU München
[2]Universität Bonn

Abstract

Grains are material regions with different lattice orientation at atomic scale. They can be resolved on material surfaces with recent image acquisition technology. Simultaneously, new microscopic simulation tools allow to study mechanical models of grain structures. The robust and reliable identification and visualization of grain boundaries - in images both from simulation and from experiments - is of central importance in the field of material surface analysis. In this work, we compare a variety of variational approaches for grain boundary estimation from microscopy and simulation images. In particular, we show that grain boundary estimation can be solved by means of recently introduced convex relaxation techniques. These techniques allow to compute global solutions or solutions within a known bound of the optimum. Moreover, experimental results both on simulated and on transmission electron microscopy images confirm that the convex relaxation techniques provide significant improvements of the estimated grain boundaries over previously employed multiphase level set formulations.

Categories and Subject Descriptors (according to ACM CCS): G.1.6 [Optimization]: Convex Relaxation, I.4.6 [Computer Vision]: Mumford-Shah Segmentation, I.6.6 [Simulation and Modelling]: Simulation Output Analysis

1. Introduction

In materials science, many important material properties can be deduced from mesoscopic quantities but the available image data lives on the atomic microscale. Thus, it is an important task in this context to extract mesoscopic quantities from microscale data. The mesoscopic quantity we focus on here are so-called *grains*, i. e. homogenous material regions with different atomic lattice orientation which are typically not in equilibrium. On the atomic microscale they are reflected in the actual positioning of neighboring atoms. To this end, image data resolved on atomic scale can be acquired by both numerical simulation models, e. g. the phase field crystal (PFC) model [EG04], and experimental tools like transmission electron microscopy (TEM) [KCF*98].

In this paper, we show that the extraction of grains from images at atomic scale can be solved by recently developed convex relaxation techniques. In particular to process images with more than two grains, the convex relaxation offers significant advantages compared to the previously employed multiphase level set method:

1. independency of initialization
2. correct encoding of the Euclidean boundary length
3. solutions within a known bound of the optimum

Furthermore, the resulting numerical algorithms are very suitable for a GPU implementation and thus allow to process a large number of images in reasonable time. For instance, this will be important in the analysis of the temporal evolution of grains boundaries in experiments and in PFC simulations.

2. Variational Estimation of Grain Boundaries

In [BRRV08], the identification of grain boundaries is modeled by a variational formulation in the spirit of the piecewise constant Mumford–Shah model [MS89]. The unknowns are a partition of Ω consisting of n regions $\Omega_1,\dots,\Omega_n$ and associated lattice orientations $\alpha_1,\dots,\alpha_n$. The corresponding energy functional is

$$E\left[(\alpha_j,\Omega_j)_{j=1}^n\right] = \sum_{j=1}^{n}\left(\int_{\Omega_j}\rho(x,\alpha_j)\,\mathrm{d}x+\frac{\lambda}{2}\,\mathrm{Per}(\Omega_j)\right), \tag{1}$$

where $\mathrm{Per}(A)$ denotes the perimeter (length of the boundary) of the set A in Ω and the so-called *indicator function* $\rho(x,\alpha)$ measures whether an angle α is an appropriate esti-

mate of the local lattice orientation at a position $x \in \Omega$ (cf. Section 2.1).

The well-known but nowadays dated approach to numerically solve this kind of segmentation problems used in [BRRV08] is the Chan–Vese model [CV01] for two phases or its multiphase extension [VC02]. In the case of two phases, the regions are described by a single level set function $\Phi : \Omega \to \mathbb{R}$ leading to the following reformulation of (1)

$$E[\alpha_1, \alpha_2, \Phi] = \int_\Omega (1 - H(\Phi(x)))\rho(x, \alpha_1) + H(\Phi(x))\rho(x, \alpha_2)\, dx + \lambda |D(H \circ \Phi)|(\Omega). \quad (2)$$

Here, H is the Heaviside function, i. e. $H(s) = 1$ for $s > 0$ and $H(s) = 0$ else, and $|Du|(\Omega)$ denotes the total variation of $u \in BV(\Omega)$. [BRRV08] uses a regularized, step size controlled gradient descent algorithm with a multi-linear FE discretization to minimize a regularized variant of (2) alternatingly minimizing with respect to the lattice orientations and the level set function. To handle more than two regions, the usage of multiple level set functions was proposed in a general context in [VC02] and adapted to grain segmentation in [BRRV08].

2.1. Construction of the Lattice Orientation Indicator ρ

In typical applications, the atom lattice underlying the input data is uniquely characterized by the neighborhood of a single atom in the lattice, i. e. the lattice is a so-called *Bravais lattice*. Therefore, the number n and the positions $q_1, \dots, q_n \in \mathbb{R}^2$ of the neighboring atoms relative to the center atom in a material reference configuration is known and fixed. Then, for a local lattice orientation $\alpha \in [0, 2\pi)$ at a particular atomic position $x \in \Omega$, the neighbors of this atom are at $x_i = x + M(\alpha(x))q_i, \quad i = 1, \dots, n$. Here, $M(\alpha)$ is a rotation by α, i. e.

$$M(\alpha) = \begin{pmatrix} cos(\alpha) & -sin(\alpha) \\ sin(\alpha) & cos(\alpha) \end{pmatrix}. \quad (3)$$

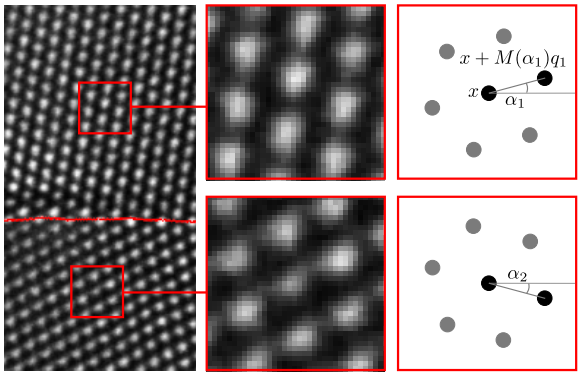

Figure 1: *Tow different local lattice orientations in a material with hexagonal packing.*

Figure 1 illustrates the scenario on a specific Bravais lattice. With this formalized lattice description we can finally define the indicator as

$$\rho(x, \alpha) := \frac{1}{\sum_{i=1}^{n} 1_{x_i \in \Omega}} \sum_{i=1}^{n} 1_{x_i \in \Omega} d(u(x), u(x + M(\alpha)q_i)), \quad (4)$$

where $d(\cdot, \cdot)$ denotes a distance function. Note that this definition slightly differs from the indicator used in [BRRV08]. The normalization factor $\frac{1}{n}$ is adjusted to account for missing neighboring atoms in the vicinity of the domain boundary. Furthermore, the formulation replaces the original thresholding based distance function by a general distance function d. In particular, this allows to consider smoother distance functions. In our experiments, it turned out that $d(a, b) = \sqrt{|a - b|}$ is most suitable for the convex reformulation.

Here, we explicitly discuss the case of hexagonal packing, but want to point out that the approach is valid for any Bravais lattice. Henceforth, we have $n = 6$ and

$$q_i := e\left(\cos\left(i\tfrac{\pi}{3}\right), \sin\left(i\tfrac{\pi}{3}\right)\right), \quad i = 1, \dots, 6, \quad (5)$$

where $e > 0$ denotes the lattice spacing. In this case, it is sufficient to consider angles $\alpha \in [0, \frac{\pi}{3})$.

2.2. Drawbacks of the Chan–Vese Approach

The Chan–Vese approach employed in [BRRV08] for the minimization of (1) has several known disadvantages motivating further improvements.

- A *local* gradient flow is used for the minimization and so the result is strongly dependent on the initialization. In particular, no optimality guarantee can be deduced.
- The regions are extracted as the intersection of the used level set functions. Thus, the number of the regions to be segmented has to be known in advance.
- When using more than two phases there are edges which are counted several times, so the Euclidean boundary length is not represented correctly (which is an inherent problem of the multi–phase Chan–Vese approach).
- Due to a gradient descent type minimization the level set approach is very costly.

Besides these drawbacks it is questionable whether the piecewise constant model is appropriate for all practical situations since there is no possibility for diffusive transitions in the lattice orientation with accompanying smoothed out edges. On the one hand, the TEM images like in Figure 3 for instance show grains surrounded by clear boundaries. On the other hand, in some of the PFC time steps (cf. Figure 4) lots of dislocations in the atom-lattice appear, boundaries get washed-out and there are smooth transitions of the lattice orientation. In the latter case, the user might not want to be restricted to piecewise constant orientations.

In the following, we give a solution for both scenarios by employing recent convex relaxation techniques.

3. Multilabel Optimization via Convex Relaxation

In a series of papers [PSG*08], [PCBC09a], [PCCB09], Pock et al. showed that optimal or near optimal solutions of multilabel optimization problems can be computed by means of Cartesian currents [GMS98] and convex relaxation techniques in the space of functions of bounded variation. We refer [AFP00] for a comprehensive introduction to BV. Here, we briefly review the results relevant in our context.

Let $u \in SBV(\Omega)$ be a function of special bounded variation, whose derivative does not contain a "spurious" contribution on sets of fractional dimension and let $\Omega \subset \mathbb{R}^2$ be the computational domain. Then the decomposition

$$Du = \nabla u \, \mathrm{d}x + (u^+ - u^-) n_u d\mathcal{H}^1_{S_u}. \tag{6}$$

holds. Here, Du denotes the measure distributional derivative of u, S_u the jump-set of u, n_u the jump-normal and $(u^+ - u^-)$ the jump-height. This motivates the definition of our general objective functional

$$\begin{aligned} F(u) = &\int_\Omega g(x, u(x), \nabla u(x)) \, \mathrm{d}x \\ &+ \int_{S_u} \psi(x, u^+, u^-, n_u) d\mathcal{H}^1, \end{aligned} \tag{7}$$

where $g : \Omega \times \mathbb{R} \times \mathbb{R}^2 \to [0, \infty]$ and $\psi : \Omega \times \mathbb{R} \times \mathbb{R} \times S^1 \to [0, \infty]$. Note that in this work we will explicitly treat functions g that are not convex in u. The splitting introduced in (6) and used in (7) allows for a different handling of the continuous and the jump-parts of u. The existence of minimizers requires assumptions on g and ψ. For a detailed existence theory, assuming the lower-semicontinuity of g and ψ, ψ only depending on $u^+ - u^-$ and the convexity of g in ∇u and ψ in $u^+ - u^-$ respectively, we refer to [Amb90].

The main idea for the convex relaxation is to express F in dependence of the graph of the characteristic function

$$1_u(x,t) : \Omega \times \mathbb{R} \to \{0,1\}, (x,t) \mapsto \begin{cases} 1 & u(x) > t \\ 0 & \text{else} \end{cases} \tag{8}$$

instead of u. Let $\Gamma_u = \partial\{1_u = 1\}$ be the extended graph of 1_u: If u is continuous, Γ_u is the classical graph of the function, otherwise one has to account in addition for the vertical jump-parts. Note that for $v = 1_u \in SBV(\Omega \times \mathbb{R})$ the first part of the decomposition (6) vanishes and apparently $S_v = \Gamma_u$ and $(v^+ - v^-) = 1$ hold. In [ABDM03], Bouchitte, Alberti and Dal Maso investigated the flux of a dual vector field, a so-called *calibration*, through the graph Γ_u. The following theorem summarizes their main result.

Theorem 3.1 For $u \in SBV(\Omega)$ it holds that

$$\begin{aligned} F(u) &= \sup_{\phi \in \mathcal{K}} \int_{\Omega \times \mathbb{R}} \phi \cdot D 1_u \\ &\overset{(6)}{=} \sup_{\phi \in \mathcal{K}} \int_{\Gamma_u} \phi \cdot n_{\Gamma_u} d\mathcal{H}^2 =: \mathcal{F}(1_u) \end{aligned} \tag{9}$$

Here, the convex set K is defined as

$$\begin{aligned} \mathcal{K} = \Big\{ &\phi = (\phi^x, \phi^t) \in \mathcal{C}_0(\Omega \times \mathbb{R}; \mathbb{R}^d \times \mathbb{R}) : \\ &\phi^t(x,t) \geq g^*(x,t,\phi^x(x,t)) \; \forall x,t \in \Omega \times \mathbb{R}, \\ &\left| \int_{t_1}^{t_2} \phi^x(x,s) ds \right| \leq \psi(x, t_1, t_2, n) \\ &\forall x, \forall t_1 < t_2, \forall n \in S^{d-1} \Big\}, \end{aligned} \tag{10}$$

and g^* is the Legendre-Fenchel conjugate of g. For a comprehensive introduction to convex analysis we refer to [ET99] and [Roc96]. The last condition on $\mathcal{K}$ limits the flux through the vertical jump-parts of u, so for $u \in W^{1,1}$ this constraint is dispensable.

Although $\mathcal{F}$ is convex in 1_u, the set $\{1_u : u \in SBV(\Omega)\}$ is not. That motivates the extension of $\mathcal{F}$ to the convex set

$$\begin{aligned} C = \Big\{ &v \in BV(\Omega \times \mathbb{R}, [0,1]) : \\ &\lim_{t \to -\infty} v(x,t) = 1, \lim_{t \to +\infty} v(x,t) = 0 \Big\}. \end{aligned} \tag{11}$$

The two limit-conditions ensure the compatibility to the original indicator functions, but C is not the convex hull of $\{1_u : u \in SBV(\Omega)\}$ since it lacks the monotonicity in t-direction. Finally, this leads to the convex minimization problem

$$\min_{v \in C} \sup_{\phi \in \mathcal{K}} \int_{\Omega \times \mathbb{R}} \phi \cdot Dv. \tag{12}$$

To make use of this convexification in practice, one still needs a connection between the relaxed and the original problem. In case the integrand in (7) is convex in Du, a generalized co-area formula

$$\mathcal{F}(v) = \int_{-\infty}^{\infty} \mathcal{F}(\chi_{v>s}) ds \tag{13}$$

is valid and allows to show that $\mathcal{F}(v) = \infty$ if v is nondecreasing in t (cf. [PCBC09b]). Here, $\chi_{v>s}$ denotes the characteristic function of the super level set $\{v > s\}$. Moreover a thresholding theorem in the spirit of Chan et al. [CEN] holds:

Theorem 3.2 Let the integrand in (7) be convex in Du, $v^* \in C$ be a solution of (12) and $s \in [0,1)$. Then $\chi_{v^*>s}$ is a global minimizer of $\mathcal{F}$ and the characteristic of a subgraph of a global minimizer of our original objective functional F.

In other words, we can obtain a solution for our original problem by solving (12) and simple thresholding. In case the original integrand is not convex in Du, such a thresholding theorem does not necessarily hold. Nevertheless, in any case, there is a bound on the optimality (adapted from the discrete label case shown in [PCCB09]):

Proposition 3.1 Let $v^* \in C$ be the global minimizer of $\mathcal{F}$ over C and $w^* \in SBV(\Omega)$ a minimizer of F over $SBV(\Omega)$. Then for any $s \in [0,1)$ one obtains

$$|\mathcal{F}(v^*) - F(w^*)| \leq |\mathcal{F}(v^*) - \mathcal{F}(\chi_{P(v^*)>s})| \tag{14}$$

holds, where P denotes the orthogonal projection on

$$\bar{C} = \{v \in C : v \text{ decreasing in } t\text{-direction}\}.$$

Note, instead of P, any other projection $C \to \bar{C}$ can be used.

Proof Because of the minimizing property of w^* and Theorem 3.1, $\mathcal{F}(1_{w^*})$ is minimal over all 1_w with $w \in SBV(\Omega)$. Furthermore, by defining $w(x) = \inf\{t : \chi_{P(v^*)>s}(x,t) = 0\}$, we get $1_w = \chi_{P(v^*)>s}$. Note that due to the projection P the mapping $\chi_{P(v^*)>s} \to w$ becomes one-to-one.
Hence, $\mathcal{F}(v^*) \le \mathcal{F}(1_{w^*}) \le \mathcal{F}(1_w) = \mathcal{F}(\chi_{P(v^*)>s})$. □

Thus, we can explicitly calculate an optimality bound for every solution. In particular, if the solution v^* is binary and decreasing in t-direction, we get a global minimizer of the original problem.

In the next section, we use the general theory to tackle the grain segmentation problem both with sharp and smooth boundaries.

4. Two Possible Energy Functionals for our Application

Let us first introduce a model that allows for smooth grain boundaries, i. e. the case not covered by the model from [BRRV08]. Picking up the indicator ρ, we define the energy

$$E_1(\alpha) := \int_\Omega \rho(x,\alpha)\,dx + \lambda |D(\alpha)|(\Omega), \tag{15}$$

where $\lambda > 0$ is a regularization parameter. In contrast to (1), we are no longer searching for an optimal partition in a finite number of grains, but for a labeling $\alpha : \Omega \to \mathbb{R}$ of our domain. The total variation is used as a regularizer for the labeling in E_1 since it is well-known for allowing jumps as well as smooth transitions. Recalling (6) and defining

$$g_1(x,\alpha,\nabla\alpha) := \rho(x,\alpha) + \lambda\|\nabla\alpha\|$$
$$\psi_1(x,\alpha^+,\alpha^-,n) := \lambda|\alpha^+ - \alpha^-|,$$

E_1 apparently is of type (7). In particular, it is convex in $D\alpha$ and we can apply the convex relaxation theory presented in Section 3 to obtain global minimizers by solving a convex optimization problem. Note that a side effect of the total variation regularization (apparent from the definition of ψ_1) is that the cost of a jump depends on the jump-height $(\alpha^+ - \alpha^-)$, cf. Figure 2. In the second half of this section, we introduce a model where the cost is independent of the jump-height.

As preparation we need to explicitly characterize the convex set $\mathcal{K}_1$ arising when applying Theorem 3.1 to E_1. For this we calculate the Legendre-Fenchel conjugate of $g_1(x,\alpha,\nabla\alpha)$ with respect to $\nabla\alpha$:

$$g_1^*(x,t,\phi^x) = -\rho(x,t) + \sup_\xi \xi\cdot\phi^x - \lambda\|\xi\|$$
$$= -\rho(x,t) + I_{\{|\phi^x|\le\lambda\}}.$$

Here, I_A is such that $I(z) = 0$ for $z \in A$ and $I(z) = +\infty$ else.

Therefore, the first condition of $\mathcal{K}_1$ implies $\|\phi^x\| \le \lambda$ and thus the second condition of $\mathcal{K}_1$, $\left|\int_{t_1}^{t_2}\phi^x(x,s)ds\right| \le \lambda|t_1 - t_2|$, is automatically fulfilled. Hence, we get

$$\mathcal{K}_1 = \left\{\phi = (\phi^x,\phi^t) : \phi^t + \rho \ge 0, \|\phi^x\| \le \lambda\right\}. \tag{16}$$

With this explicit description of $\mathcal{K}_1$ and using Theorems 3.1 and 3.2, we can find global minimizers of E_1 by minimizing the convex function

$$\mathcal{F}_1(v) := \sup_{\phi\in\mathcal{K}_1} \int_{\Omega\times\mathbb{R}} \phi\cdot Dv \tag{17}$$

over the convex set C and thresholding the solution at 0.5.

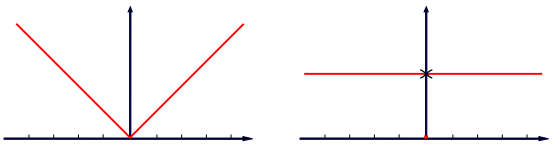

$$\psi_1(x) = |x| \qquad \psi_2(x) = \begin{cases} 1 & x \ne 0 \\ 0 & \text{else} \end{cases}$$

Figure 2: *Two popular interaction potentials: While the TV regularizer (left) penalizes the size of the jump linearly, the Potts model (right) imposes a constant penalty for all discontinuities.*

To model sharp grain boundaries, we want to use the piecewise constant Mumford–Shah model, similarly to [BRRV08]. Unfortunately, g is independent of $\nabla\alpha$ for this model, thus $g^* \equiv \infty$ and the approach from Section 3 cannot be applied directly. To bypass this limitation, we apply the convexification to the full Mumford–Shah functional using the indicator ρ, i. e.

$$\tilde{E}_2(\alpha) := \int_\Omega \rho(x,\alpha)\,dx + \nu\int_{\Omega\setminus S_\alpha} \|\nabla\alpha\|^2\,dx + \lambda\mathcal{H}^1(S_\alpha). \tag{18}$$

This convexification of this special type of functionals was considered in [PCBC09a]. With

$$g_2(x,\alpha,\nabla\alpha) := \rho(x,\alpha) + \nu\|\nabla\alpha\|^2$$
$$\psi_2(x,\alpha^+,\alpha^-,n) := \begin{cases} \lambda & \alpha^+ \ne \alpha^- \\ 0 & \text{else} \end{cases},$$

$\tilde{E}_2$ is of type (7), but not convex in $D\alpha$. The discrete, non-convex interaction potential corresponding to $\mathcal{H}^1(S_\alpha)$ is the Potts model, see Figure 2 for a comparison of this potential with the TV potential. In particular, let us point out that the cost of a jump in this model does not depend on the jump-height.

The Legendre-Fenchel conjugate is

$$g_2^*(x,t,\phi^x) = -\rho(x,t) + \sup_{\xi} \xi\cdot\phi^x - \nu\|\xi\|^2$$
$$= -\rho(x,t) + \tfrac{\|\phi^x\|^2}{4\nu}.$$

and the convex set necessary for Theorem 3.1 is

$$\tilde{\mathcal{K}}_2 = \Big\{\phi=(\phi^x,\phi^t) : \phi^t \geq -\rho + \tfrac{\|\phi^x\|^2}{4\nu}, \Big|\int_{t_1}^{t_2}\phi^x ds\Big| \leq \lambda, \forall t_1 < t_2\Big\}. \tag{19}$$

Note that the second constraint of this set is not redundant for $\tilde{E}_2$. Heuristically applying the limit $\nu\to\infty$ in $\tilde{\mathcal{K}}_2$ and in the functional corresponding to $\tilde{E}_2$ from Theorem 3.1 and tightening the resulting first constraint of $\tilde{\mathcal{K}}_2$ to $|\phi^t|\leq\rho$, leads to

$$\mathcal{K}_2 = \Big\{\phi=(\phi^x,\phi^t) : |\phi^t|\leq\rho, \Big|\int_{t_1}^{t_2}\phi^x ds\Big| \leq \lambda, \forall t_1 < t_2\Big\} \tag{20}$$

and

$$\mathcal{F}_2(v) := \sup_{\phi\in\mathcal{K}_2}\int_{\Omega\times\mathbb{R}} \phi\cdot Dv. \tag{21}$$

Based on similar arguments as in the proof of Theorem 3.1, one shows $\mathcal{F}_2(1_\alpha) = E_2(\alpha)$ for all $\alpha\in SBV$, where

$$E_2(\alpha) = \begin{cases} \int_\Omega \rho(x,\alpha)\,dx + \lambda\mathcal{H}^1(S_\alpha) & \alpha \text{ pcw. const.} \\ \infty & \text{else.}\end{cases}$$

Therefore, if α is piecewise constant, $\mathcal{F}_2(1_\alpha)$ is the same as (1), the piecewise constant Mumford–Shah functional for grain segmentation.

The tightening of the first bound is inspired by [CCP08]: Due to the lack of convexity of g in $D\alpha$, solutions of the "untightened" problem are not necessarily decreasing in t-direction. The central idea of [CCP08] is a slight modification of the objective function, which in our case results in the aforementioned tightening. Based on this, [CCP08] shows that minimizers of the discrete counterpart of $\mathcal{F}_2$ always fulfill the monotonicity, cf. [CCP08, Proposition 4.3].

As discussed earlier, due to the non-convexity of E_2 in $D\alpha$ we cannot guarantee that minimizing $\mathcal{F}_2$ over C and thresholding leads to a global minimizer of E_2. But because of $\mathcal{F}_2(1_\alpha) = E_2(\alpha)$, the error bound from Proposition 3.1 still holds.

5. Numerical Implementation

The two convex functions corresponding to grain segmentation with smooth (17) and sharp (21) boundaries, lead to two almost identical optimization problems, i. e.

$$\inf_{v\in C}\sup_{\phi\in\mathcal{K}_i}\int_\Omega \phi\cdot Dv, \quad i=1,2.$$

Both are saddlepoint problems only differing in the convex set used for the supremum. To solve such problems, we use a simple primal-dual projected gradient ascent/descent scheme related to [Pop80] and [ZC08]. A convergence result was recently established in [PCBC09a]. The main idea is to alternate simple unconstrained gradient steps in v and ϕ where each gradient step is followed by a projection onto the corresponding convex set (C or $\mathcal{K}_i$). The step sizes are chosen corresponding to [PCBC09a, Theorem 2] and the so-called *primal-dual-gap* is used as stopping criterion. The spatial discretization uses a simple uniform rectangular grid. The gradient descent steps on such a grid are highly parallelizable, so we could create an efficient GPU implementation of the algorithm.

Although the implementation for both problems is almost the same, the runtime differs considerably. The bottleneck in both variants is the projection on $\mathcal{K}_i$. While the projection on $\mathcal{K}_1$ can be computed pointwise and thus efficiently, because the constraints therein are local, the projection on $\mathcal{K}_2$ is much more involved due to the non-local constraint $|\int_{t_1}^{t_2}\phi^x ds|\leq\lambda$. In particular, this constraint complicates an efficient parallel implementation. Here, we employed the method of Dykstra [BD86] to handle the projection. Overall, almost 90% of the computing time is consumed by the projection on $\mathcal{K}_2$.

6. Experimental Results

In the following, we present experimental results of the proposed models. We first consider $\mathcal{F}_1$ and $\mathcal{F}_2$ separately and conclude this section with a comparison of both models to the Chan–Vese formulation of (1). To compare the smooth boundary model to the Chan–Vese model, we also investigate to which extend accurate sharp boundaries can be obtained by clustering results in the model which also allows for smooth transitions in the orientation.

6.1. Results with Total Variation Regularity

To get started, we use $\mathcal{F}_1$ to label a simple TEM image only showing two clearly separated grains, see Figure 3. The regions of uniform lattice orientation in the upper left and lower right part of the TEM image are clearly recognized

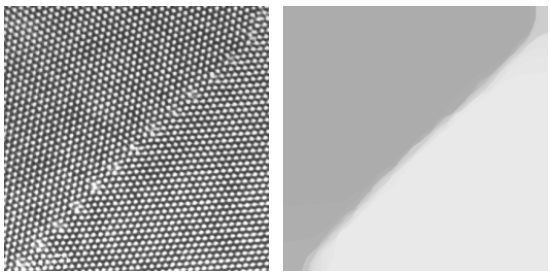

Figure 3: *TEM input image (left) and labeling α^* obtained with $\mathcal{F}_1$ (right)*

with some fuzziness in the boundary region. This fuzziness has a clear physical correspondence: In the vicinity of the boundary are several impurities caused by dislocations in the atomic lattice. Furthermore, note that one can only assign a valid lattice orientation to positions at least one atom distance away from the grain boundary.

Since PFC simulations usually show more and smaller grains than TEM images, we focus on PFC data in the remainder of the section. Figure 4 shows a first result using

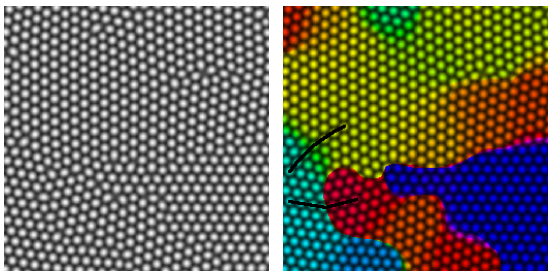

Figure 4: *PFC input image (left) and colored visualization of the labeling obtained with $\mathcal{F}_1$ (right), in the latter one smooth and one sharp lattice orientation transitions is marked with black lines.*

$\mathcal{F}_2$ on a PFC image. To facilitate the visualization of the obtained global optimal labeling α^* its values were mapped to a periodic HSV-colorspace and alpha-blended to the input data. Note that the periodicity of the colorspace is necessary to color similarly oriented lattices regions with similar hues. The obtained labeling accurately captures the lattice geometry. The algorithm even manages to extract information, that is not easily visible to an untrained human eye. To outline that the total variation regularization used in E_1 allows for smooth transitions and sharp edges, one smooth and one sharp orientation transitions is marked in the image showing the labeling.

6.2. Results with Potts Regularity

Results of using our sharp interface energy $\mathcal{F}_2$ using two different values of λ are shown in Figure 5. In order to compare the results of the smooth and the sharp mode, we use the same PFC input image as in Figure 4. The bigger lambda, the more small regions are merged to bigger ones since the λ-weighted boundary length cost exceeds the gain by better data fitting. Thus, λ allows to choose a preferred scale and to select the smallest grain size we want to visualize. This can also be interpreted as a way to chose the number of regions in (1) dynamically.

Furthermore, as the equivalent of Proposition 3.1 for $\mathcal{F}_2$ holds (cf. Section 4), we are able to calculate an optimality bound. Because the overall energy of the solution depends on the scale parameter, the discretization and the size of the

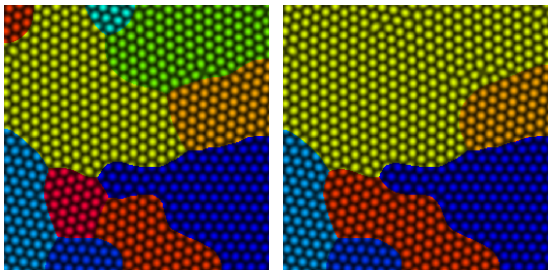

Figure 5: *Results on the PFC image from Figure 4 obtained with $\mathcal{F}_2$ using two different values of the regularization parameter λ. When increasing the regularization (left to right), small grains are merged to bigger ones.*

image, we normalize the gap (14) and fix 0.5 as threshold parameter s:

$$\varepsilon_{opt} := \frac{\mathcal{F}_2(\chi_{\{P(v^*)>0.5\}}) - \mathcal{F}_2(v^*)}{\mathcal{F}_2(v^*)}. \tag{22}$$

So ε_{opt} is a quality measure for the obtained solution. For all our experiments we found ε_{opt} to be less than 1%.

Finally, let us emphasize that both results nicely comply with the following theoretical property of the Mumford–Shah model [MS89].

Proposition 6.1 Edges of minimizers of the piecewise-constant Mumford–Shah functional are perpendicular to $\partial\Omega$ and meet in the interior exclusively at triple points with pairwise angle of 120°.

6.3. Comparison with the Chan–Vese Level Set Method

To conclude the numerical results, we compare the results of our two models and the classical approach on a large PFC image with a large number of different grains, cf. Figure 6 (left). The need for a good visualization to capture all relevant information and to evaluate the state of the crystal simulation from this kind of image is apparent. Small changes in the lattice orientation are almost not visible and the classification with grains having the same or similar orientations is very difficult for the human eye. The middle image of Figure 6 shows the segmentation in eight (2^3) grains using three level set functions obtained with the classical multiphase Chan–Vese approach, cf. [Ber10, Figure 3.14]. Due to the locality of the optimization method and the wrong encoding of the Euclidean boundary length in the multiphase model the result is neither a global minimizer of (1) nor can an optimality bound like in Proposition 3.1 be assumed to hold. Furthermore, unlike our result obtained with $\mathcal{F}_2$ (right image in Figure 6), it does not satisfy the properties from Proposition 6.1. Nevertheless, qualitatively both methods find similar grains, especially the larger ones. However, clearly wrong in the Chan–Vese based result is the appearance of small grains with a width of about one atom: The data term cannot

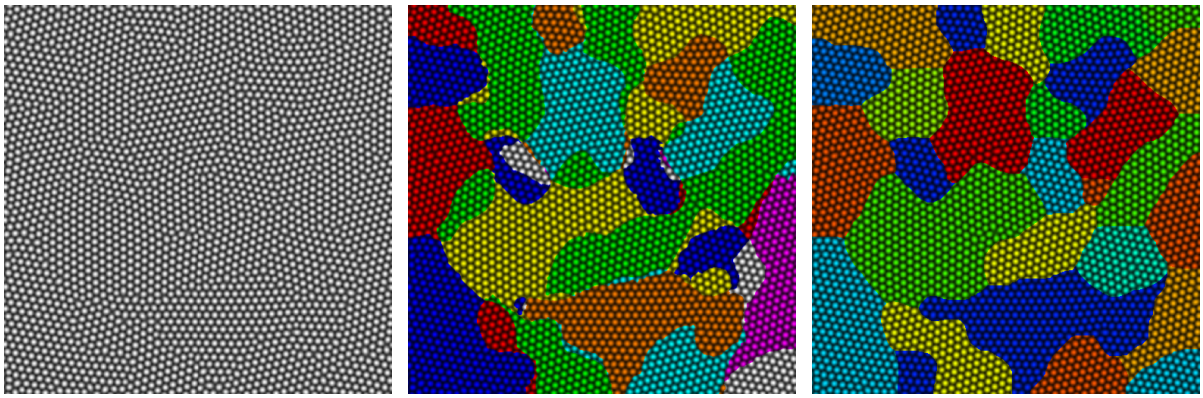

Figure 6: *PFC input image (left), segmentation in eight grains obtained via the classical Chan–Vese approach (middle, result from [Ber10, Figure 3.14]) and our result by using $\mathcal{F}_2$, the proposed convex relaxation for sharp boundaries (right).*

assign a valid orientation here, thus the penalization of the boundary length in the Mumford–Shah model should have eliminated these regions.

Figure 7 (left) shows the lattice orientation labeling obtained using our smooth boundary model on the PFC image from Figure 6. This model correctly identifies the smooth orientation transitions present in the PFC image whereas the sharp model (Figure 6, right) by design has to put grain boundaries even where no jump in the orientation is present (cf. the boundary between green and yellow in the middle of the image). The already mentioned global optimality of the smooth model aside, another advantage of $\mathcal{F}_1$ is that the resulting smooth labeling can be converted to a segmentation with sharp boundaries using simple k-means clustering as postprocessing. Figure 7 (middle and right) depicts results of such a clustering in 5 and 8 segments. Even this produces segmentations that are quite comparable to the results of the multiphase Chan–Vese approach and has the additional advantage that the k-means clustering can be done very quickly for different numbers of cluster.

Because of the different architectures used and the high dependence on discretization, step size, termination criterion, etc., the runtime of our proposed algorithms and the multiphase Chan–Vese approach cannot be directly compared. Our GPU-implementation with a fast, highly parallel, primal-dual algorithm needed 105 seconds (512^2 pixles) for the TV regularization in Figure 7 and about 8 minutes for the Potts regularization in Figure 6, the runtime k-means-clustering can be neglected. The runtime for the Chan–Vese optimization was more than one hour using a single CPU implementation.

7. Conclusion

In this paper, we propose the application of convex relaxation techniques to the extraction and visualization of grain boundaries from TEM and PFC images. Two variational formulations dependent on the purpose of postprocessing are introduced and compared to the multiphase Chan–Vese approach. In contrast to the latter, in case of TV regularization (smooth boundary model) the global optimal solution is found and in case of Potts regularity (sharp boundary model) a tight bound for optimality is obtained. Moreover, the results in the experimental section indicate that the new methods significantly outperform the previous ones also for practical purposes.

For future work we mainly see two directions. One direction is to extend the approach from images to videos, interpreting successive time steps of a PFC simulation as video. In order to visualize the formation and disintegration of grain boundaries it could be useful to enforce a temporal regularity on the lattice labeling. The other direction is to develop even more efficient algorithms and to push the runtime of the TV regularizer towards “almost” realtime.

References

[ABDM03] ALBERTI G., BOUCHITTÉ G., DAL MASO G.: The calibration method for the Mumford-Shah functional and free-discontinuity problems. *Calculus of Variations and Partial Differential Equations 16*, 3 (2003), 299–333. 3

[AFP00] AMBROSIO L., FUSCO N., PALLARA D.: *Functions of bounded variation and free discontinuity problems*. Oxford Mathematical Monographs. Oxford University Press, New York, 2000. 3

[Amb90] AMBROSIO L.: Existence theory for a new class of variational problems. *Archive for Rational Mechanics and Analysis 111*, 4 (1990), 291–322. 3

[BD86] BOYLE J., DYKSTRA R.: A method for finding projections onto the intersections of convex sets in Hilbert

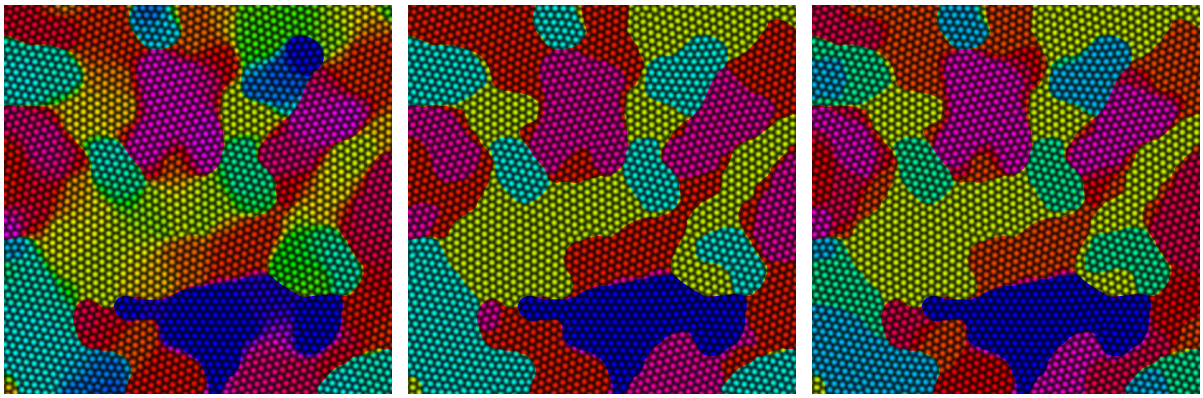

Figure 7: *Labeling of the PFC image from Figure 6 obtained with the smooth interface energy $\mathcal{F}_1$ (left) and k-means clustering of this labeling in* 5 *(middle) and* 8 *(right) regions.*

spaces. In *Advances in order restricted statistical inference: proceedings of the Symposium on Order Restricted Statistical Inference, Iowa City, Iowa, September 11-13, 1985* (1986), Springer Verlag, p. 28. 5

[Ber10] BERKELS B.: *Joint methods in imaging based on diffuse image representations*. Dissertation, University of Bonn, 2010. 6, 7

[BRRV08] BERKELS B., RÄTZ A., RUMPF M., VOIGT A.: Extracting grain boundaries and macroscopic deformations from images on atomic scale. *Journal of Scientific Computing 35*, 1 (2008), 1–23. 1, 2, 4

[CCP08] CHAMBOLLE A., CREMERS D., POCK T.: *A convex approach for computing minimal partitions*. Sekretariat für Forschungsberichte, Institut für Informatik III, Universität Bonn, 2008. 5

[CEN] CHAN T., ESEDOGLU S., NIKOLOVA M.: Algorithms for finding global minimizers of image segmentation and denoising models. *Algorithms 66*, 5, 1632–1648. 3

[CV01] CHAN T. F., VESE L. A.: Active contours without edges. *IEEE Transactions on Image Processing 10*, 2 (2001), 266–277. 2

[EG04] ELDER K. R., GRANT M.: Modeling elastic and plastic deformations in nonequilibrium processing using phase field crystals. *Physical Review E 70*, 5 (November 2004), 051605–1–051605–18. 1

[ET99] EKELAND I., TEMAM R.: *Convex analysis and variational problems*. Society for Industrial Mathematics, 1999. 3

[GMS98] GIAQUINTA M., MODICA G., SOUČEK J.: *Cartesian Currents in the Calculus of Variations: Variational integrals*. Springer Verlag, 1998. 3

[KCF*98] KING W. E., CAMPBELL G. H., FOILES S. M., COHEN D., HANSON K. M.: Quantitative HREM observation of the $\Sigma 11(113)/[\bar{1}00]$ grain-boundary structure in aluminium and comparison with atomistic simulation. *Journal of Microscopy 190*, 1 (1998), 131–143. 1

[MS89] MUMFORD D., SHAH J.: Optimal approximation by piecewise smooth functions and associated variational problems. *Communications on Pure Applied Mathematics 42* (1989), 577–685. 1, 6

[PCBC09a] POCK T., CREMERS D., BISCHOF H., CHAMBOLLE A.: An algorithm for minimizing the Mumford-Shah functional. In *ICCV Proceedings* (2009). 3, 4, 5

[PCBC09b] POCK T., CREMERS D., BISCHOF H., CHAMBOLLE A.: Global solutions of variational models with convex regularization. *Preprint* (2009). 3

[PCCB09] POCK T., CHAMBOLLE A., CREMERS D., BISCHOF H.: A convex relaxation approach for computing minimal partitions. 3

[Pop80] POPOV L.: A modification of the Arrow-Hurwicz method for search of saddle points. *Mathematical Notes 28*, 5 (1980), 845–848. 5

[PSG*08] POCK T., SCHOENEMANN T., GRABER G., BISCHOF H., CREMERS D.: A convex formulation of continuous multi-label problems. *Computer Vision–ECCV* (2008), 792–805. 3

[Roc96] ROCKAFELLAR R.: *Convex analysis*. Princeton Univ Press, 1996. 3

[VC02] VESE L., CHAN T.: A multiphase level set framework for image segmentation using the Mumford and Shah model. *International Journal of Computer Vision 50*, 3 (2002), 271–293. 2

[ZC08] ZHU M., CHAN T.: An efficient primal-dual hybrid gradient algorithm for total variation image restoration. *UCLA CAM Report* (2008), 08–34. 5